Dispersive and dispersive-like bores in channels with sloping banks

Rémi Chassagne, Andrea Gilberto Filippini, Mario Ricchiuto, Philippe Bonneton

Dispersive and dispersive-like bores in channels with sloping banks

R. Chassagne , A.G. Filippini, M. Ricchiuto, P. Bonneton

Dispersive and dispersive-like bores in channels with sloping banks

R. Chassagne [*], A.G. Filippini[†], M. Ricchiuto[‡], P. Bonneton[§]

Project-Team CARDAMOM

Abstract: In this paper, a detailed analysis of undular bore dynamics in channels of variable cross-section is presented. Two undular bore regimes, Low Froude Number (LFN) and High Froude Number (HFN), are simulated with a Serre-Green-Naghdi model, and the results are compared with the experiments by Treske. We show that contrary to Favre waves and HFN bores, which are controlled by dispersive non-hydrostatic mechanisms, LFN bores correspond to a hydrostatic phenomenon. The dispersive-like properties of the LFN bores is related to wave refraction on the banks in a way similar to that of edge waves in the nearshore. A fully hydrostatic theoretical model allowing to describe these dispersive-like bores is derived and compared to the observations, confirming our claim.

Key-words: Long waves, dispersive effects, Froude number, channels, asymptotic analysis, Serre-Green-Naghdi equations, Dispersive shock, Tidal bores

[*] Univ. Grenoble Alpes, Irstea, ETNA, 38000 Grenoble, France
[†] University of Bordeaux, CNRS, UMR 5805 EPOC, Allée Geoffroy Saint-Hilaire, F-33615 Pessac, France
[‡] eam CARDAMOM, Inria Bordeaux - Sud-Ouest, 200 Avenue de la Vieille Tour, 33405 Talence cedex, France
[§] University of Bordeaux, CNRS, UMR 5805 EPOC, Allée Geoffroy Saint-Hilaire, F-33615 Pessac, France

Dispersive-like waves

Résumé :   Dans cet article, une analyse détaillée de la dynamique des ressauts undulaires dans des canaux de section variable est présentée. Des régimes Low Froude Number (LFN) et High Froude Number (HFN), sont simulés avec un modèle Serre-Green-Naghdi et les résultats sont comparés aux expériences de Treske. Nous montrons que, contrairement aux ondes Favre et aux ondes HFN, contrôlés par des mécanismes dispersifs non hydrostatiques, les ondes LFN correspondent à un phénomène hydrostatique. Les propriétés de dispersion des ressauts LFN sont liées en effet à la réfraction des vagues sur les berges, de la même manière que les edge waves. Un modèle théorique hydrostatique permettant de décrire ces ondes "dispersive-like" est dériv et comparé aux observations, confirmant ainsi notre hypothèse.

Mots-clés :   ondes longues, effets dispersifs, nombre de Froude, analyse asymptotique, modeles Serre-Green-Naghdi, choc dispersifs

Contents

1 Introduction

A bore is a propagating transition between two streams with different water depths h_1 and h_2 ($h_1 < h_2$). The intensity of two-dimensional (vertical plane) bores is mainly characterized by the Froude number $Fr = |u_1 - c_b|/\sqrt{gh_1}$, where u is the depth averaged velocity and c_b the bore celerity. For large Fr the transition corresponds to a turbulent breaking zone of water. For Fr smaller than about 1.3, the bore transition is smooth and followed by wave trains. The bore is hence made of a mean jump between two water depths on which secondary waves are superimposed. This type of bore is usually named *undular bore*. [11] was the first to describe this phenomenon from laboratory experiments. That is why undular bores are sometimes referred to *Favre waves*. This phenomenon is a weakly dispersive non-hydrostatic process which can be modeled by Boussinesq-type equations (e.g. [23]). In the mathematical community this dispersive process is also named *dispersive shock*. The dynamics of two-dimensional undular bores has been extensively studied from laboratory experiments [**?**, e.g.]]favre1935,treske1994,soaresfrazao2002,chanson2009, theoretical [**?**, e.g.]]lemoine1948,benjamin1954,johnson1972,el2006 and numerical approaches [23, 31, **?**, 27, 17].

However, natural estuary and river channels are non rectangular and present most of the time a variable cross-section with gently sloping banks (see figure 1). The bore dynamics is then mainly controlled by three dimensionless parameters:

$$Fr = |U_1 - c_b|/\sqrt{g\bar{h}_1}, \qquad W/h_1, \qquad \tan\beta,$$

where U is the cross-sectionally averaged velocity, $\bar{h}$ the cross-sectionally averaged water depth, W and β are the characteristic bottom channel width and bed-slope angle from horizontal respectively. Only a few studies have been devoted to undular bore dynamics in channels with variable cross-section. The propagation of undular bores over a trapezoidal cross-section channel, with fixed parameters $\beta = 1/3$ and $W/h_1 = 7.75$, was studied by [29]. He showed that the secondary

wave field is three-dimensional with strong variations in crest height across the channel section, and then strongly differs from that in rectangular channels. [29] identified a transition around $Fr_t = 1.15$. For $F < Fr_t$, the secondary wave wavelength in the whole channel is at least two to three times larger than in a rectangular channel for same Froude numbers. For $F > Fr_t$ however the secondary wave field long the channel axis becomes very similar to Favre waves (rectangular channels), while long wave lengths are still observed along the banks, leading to a complex three-dimensional wave structure. In field observations a similar three-dimensional structure was described for the first time in long-term high-frequency experiments carried out in the two main French tidal bore estuaries: the Seine and Gironde/Garonne estuaries (see [6, 2, 4]). The authors identified two undular bore regimes around a transition Froude number Fr_t of about 1.1: the high Froude number regime (HFN regime) for $F > Fr_t$ and the low Froude number regime (LFN regime) for $F < Fr_t$. In the HFN regime, the secondary wave field is strongly three-dimensional and characterized by a "fish-tail" pattern (see figure2-(a)). The wave amplitude is maximum in the mid-channel and decreases toward the banks (figure2-(b)). It was shown that the amplitude and wavelength along the river axis are similar to that of Favre waves in rectangular channels for the same Froude number. This observation indicates that this HFN regime is most probably controlled by dispersive non-hydrostatic processes as for the Favre waves. The secondary wave field in the LFN regime shows a significantly different behaviour. The phase structure is quasi one-dimensional (figure2-(c)) and the wave amplitude is maximum on the banks and minimum in the mid-channel (figure2-(d)). The transition between HFN and LFN regimes is marked by an abrupt decrease of the secondary wave steepness ([4]), and by a considerable increase in wave length. The low wave steepness of the LFN makes visual observations of undular tidal bores very difficult. This is why tidal bore occurrence in worldwide estuaries is certainly underestimated ([5, 4]).

In this paper, a detailed analysis of undular bore dynamics in channels of variable cross-section is presented. The two undular bore regimes (LFN and HFN) are simulated with a Serre-Green-Naghdi model, and the results are compared with Treske's experiments. We show that contrary to Favre waves and HFN bores, which are controlled by dispersive non-hydrostatic mechanisms, the LFN bores correspond to an hydrostatic phenomenon. The dispersive-like properties of the LFN bores is related to wave refraction on the banks in a way similar to that of edge waves in the nearshore. A fully hydrostatic theoretical model allowing to describe the dispersive-like bores (i.e. LFN bores) is derived and compared to the observations, confirming our claim.
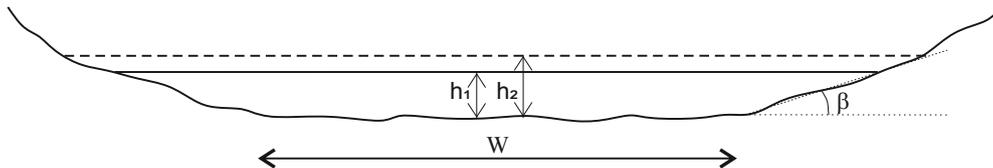
Figure 1: Schematic representation of the cross-section of natural alluvial channels. W is the bottom channel width, β the bed-slope angle from horizontal, h_1 and h_2 are the water depths ahead and behind the bore respectively.
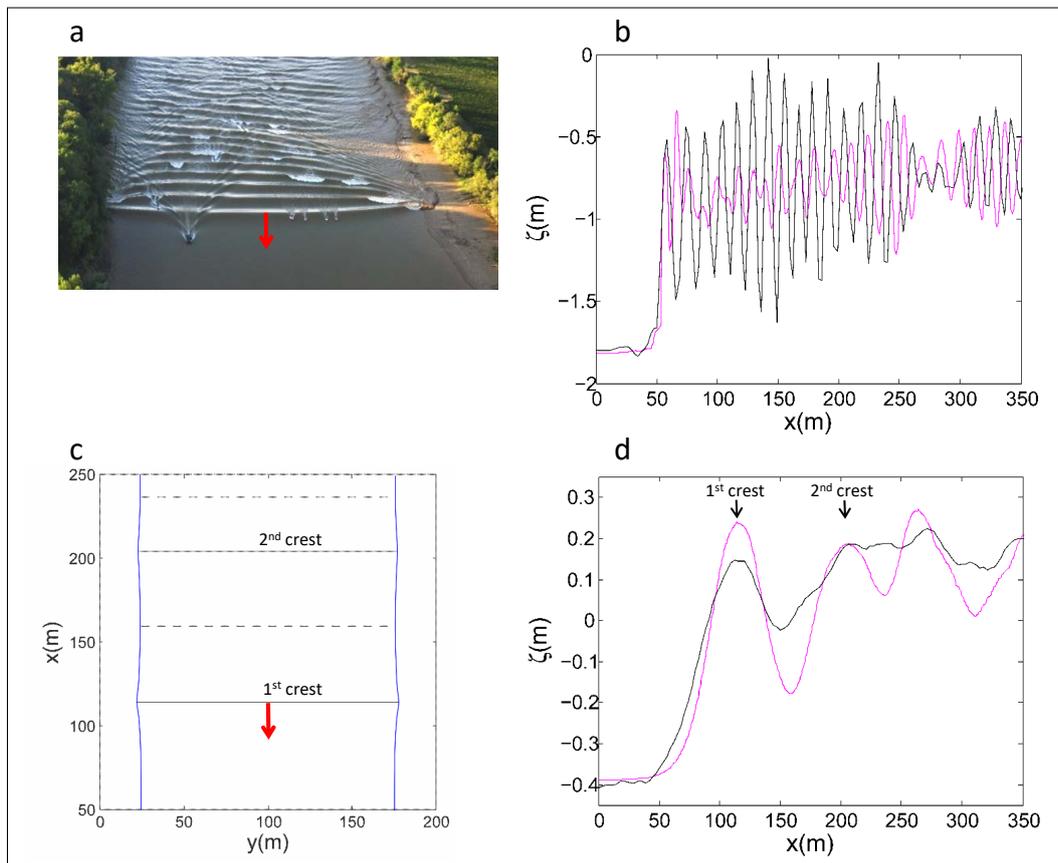
Figure 2: Illustration of the two undular tidal bore regimes (Garonne River, [4]). (a), (b): high Froude number regime (Fr=1.27); (c), (d): low Froude number regime (Fr=1.08). (a): 2D phase structure ; (c): quasi-1D phase structure. Black line, elevation in the mid-channel; Magenta line, elevation close to the bank.

2   Dispersive wave modelling

2.1   Mathematical and numerical model

The generation of undular bores is in general related to non-hydrostatic propagation and thus it requires the use of dispersive equations to be correctly modelled. In this work we use a phase-enhanced fully nonlinear and weakly dispersive Serre-Green-Naghdi model which can be recast as [12, 13]:

$$\frac{\partial \zeta}{\partial t} + \nabla \cdot \big(h\boldsymbol{u}\big) = 0$$

$$\frac{\partial \big(h\boldsymbol{u}\big)}{\partial t} + \nabla \cdot \big(h\boldsymbol{u} \otimes \boldsymbol{u}\big) + gh\nabla\zeta = \boldsymbol{\phi} \tag{1}$$

where ζ denotes the free surface elevation, h the water depth, and $\boldsymbol{u}$ the depth averaged horizontal velocity vector of $\boldsymbol{u} = (u, v)$. The term $\boldsymbol{\phi}$ represents the non-hydrostatic effects, and can be shown to be the solution of an auxiliary elliptic partial differential equation which can be written as

$$\boldsymbol{\phi} + \alpha\mathrm{T}\big(\boldsymbol{\phi}\big) \; = \; \mathrm{T}\Big(gh\nabla\zeta\Big) - \mathrm{Q}(\boldsymbol{u}) \; ; \tag{2}$$

where α is a tuning parameter allowing to enhance the linear frequency dispersion and shoaling characteristics of the model [8], with optimal value $\alpha = 1.159$. The definitions of the differential operators $\mathrm{T}(\boldsymbol{\omega})$ and $\mathrm{Q}(\boldsymbol{\omega})$ are reported for completeness in the appendix, following [20, 12, 13]. For $\boldsymbol{\phi} = 0$ the system reduces to the hydrostatic, hyperbolic Saint-Venant/shallow water model.

The coupled system (1)-(2) is solved numerically on unstructured grids using the two step hybrid strategy proposed in [12, 13]. In this approach the first step consists in recovering the non-hydrostatic correction by solving the elliptic problem (2) using a finite element method based on the symmetric variational form exploiting the self-adjoint character of the operator T (see [12, 1] for details). Once ϕ is known, the evolutionary partial differential equations (1) are solved by means of a third-order finite volume method, combined with a third order SSP Runge-Kutta or with a fourth order Adams-Bashforth/Adams-Moulton predictor corrector method to march in time. The resulting algorithm has been shown to have discrete linear dispersion properties comparable to those of a fourth order finite difference discretization [12, 14].

Finally, wave breaking is modelled by means of the shock capturing approach also used in [28, 26, 16, 24, 12]: the non-hydrostatic correction $\boldsymbol{\phi}$ is set to zero in regions a-priori flagged as breaking. This allows for the formation of dissipative bores/shocks across which the total energy is dissipated, with a rate very close to the one encountered in the surf region [3]. The flagging is performed by means of the physical criteria suggested in [16], which make use of the norm of the gradient of the time derivative of the free surface ζ, and of a limiting of the breaking region based on a minimum local Froude number of roughly 1.3 as proposed in [26].

2.2   Numerical Validation

Even though the approach described in the previous section has been thoroughly validated in the original references, we present here a preliminary application of the model to a case relevant for our study: the formation of undular bores in channels with a rectangular section. Experiments were conducted by [11] and [29]. Numerical simulations with one dimensional Serre-Green-Naghdi model were also performed in [25].

(a)

(b)
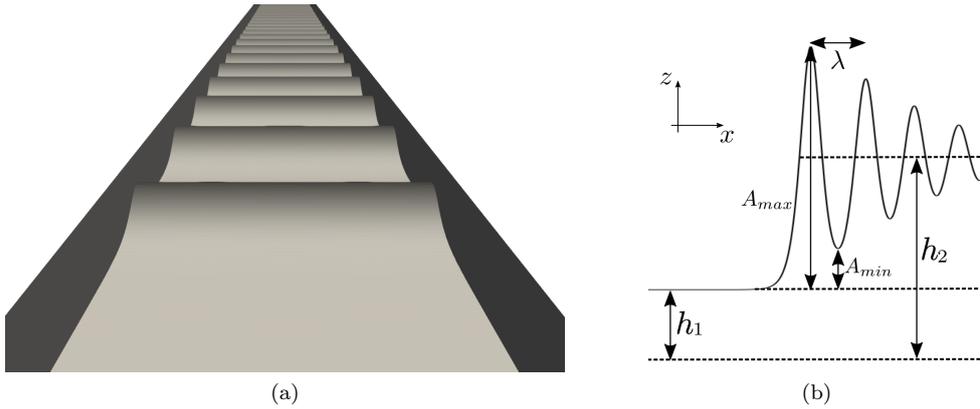
Figure 3: Bore in a channel of rectangular section. (a): Typical free surface distribution obtained numerically, (b): Physical parameters measured

The initial solution for this simulation is based on the mean hydrostatic bore solution, which satisfies the Rankine-Hugoniot relations associated to the Saint-Venant system. Denoting the states ahead and behind the bore with subscripts 1 and 2, these conditions read:

$$\begin{cases} u_1 - c_b = -\left(\dfrac{gh_2}{2h_1}(h_1 + h_2) \right)^{1/2} \\ \\ u_2 - c_b = -\left(\dfrac{gh_1}{2h_2}(h_1 + h_2) \right)^{1/2} \end{cases} . \tag{3}$$

The numerical simulations are done in the same configuration than the experiments of [29] with $u_1 = 0$ m/s and $h_1 = 0.16$ m, on a rectangular computational domain of dimensions $[100 \times 2]$ m^2, and with the following regularization of the initial discontinuity:

$$\begin{cases} h(x, y, t = 0) &=& \dfrac{h_2 - h_1}{2} \tanh\left((x - x_0)/l_t\right) + h_2 \\ \\ u(x, y, t = 0) &=& \dfrac{u_2 - u_1}{2} \tanh\left((x - x_0)/l_t\right) + u_2 \\ \\ v(x, y, t = 0) &=& 0 \end{cases} , \tag{4}$$

where $x_0 = 95$ m and $l_t = 0.5$ m. The reference grid sizes in the longitudinal and transversal axis are $\delta_x = 0.04$ m and $\delta_y = 0.5$ m. This discretization has been chosen to have always at least twenty grid points per wavelength. Periodic boundary conditions are used in the y direction.

Several simulations have been run for values of the Froude number $Fr = |u_1 - c_b|/\sqrt{gh_1}$ from 1.01 to 1.30, below the onset of wave breaking. On figure 3-(a) we report a visualization of the typical free surface profile obtained numerically. The quantities compared to the experimental data of [29] and [11] are the wavelengths and heights A_{max} and A_{min} sketched on figure 3-(b). The comparisons are reported on figure 4.

Despite a small overestimation, the model predicts well the long waves for small Froude numbers and the wavelength reduction for increasing Fr. The water level elevations A_{max} and A_{min} fit very well the data of [29] and [11]. For completeness we also report on figure 4-(a) the

(a) Wavelength

(b) Water level elevation
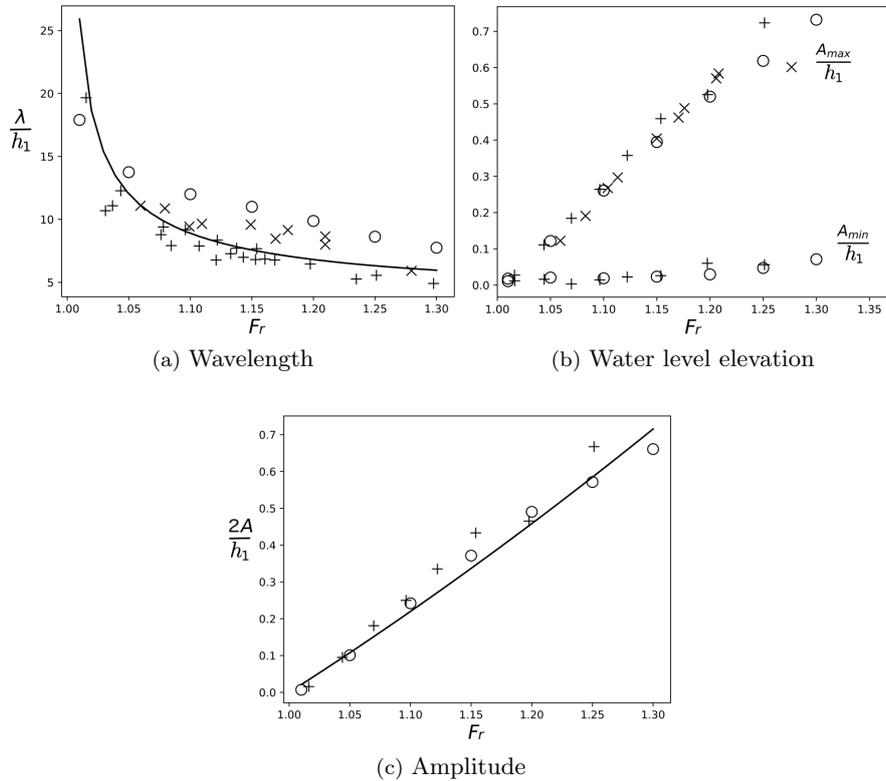
(c) Amplitude

Figure 4: Undulating bores in channel with rectangular section: wavelength (left), water heights (middle), and amplitude (right). $+$: Data of [29], $\times$: [11], $\circ$: numerical simulations, $-$: [21] theory.

wavelengths predicted by the well known theory by [21] around which the experimental results cluster quite closely. Finally, figure 4-(c) compares the wave height $2A := A_{max} - A_{min}$ obtained numerically against the experimental values by [29] and the theoretical values by [21]. The agreement is again very good. For a Froude number higher than 1.30, the transition to breaking occurs. For numerical results in this regime we refer to [17] and [25].

3   Bore propagation in trapezoidal channels

In the last section it has been recalled that the secondary wave field in rectangular channel is a dispersive non-hydrostatic phenomenon (a dispersive shock). As discussed in the introduction, the bore dynamics drastically change when topographic variations along the channel cross-section are present, as shown by [29] in laboratory experiments, and by [4] in field observations. To show that we can model these dynamics with a weakly dispersive Serre-Green-Naghdi approach, in this section we reproduce numerically the experiments by Treske. As we will see, the simulations allow to reproduce the transition between the High Froude Number (HFN) and Low Froude Number (LFN) regimes discussed in the introduction. The comparison between simulations and experimental data allows to gain some further insight in the differences between these two regimes,

(a) Cross view   (b) Lateral view
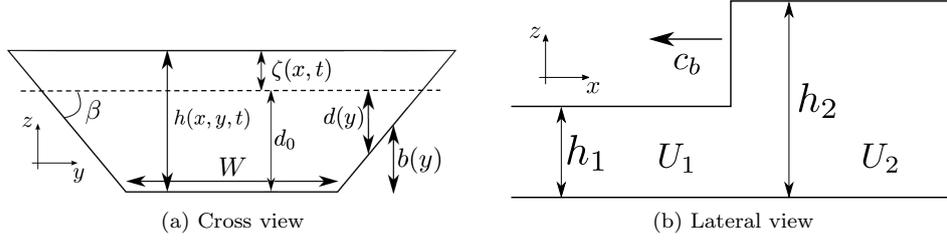
Figure 5: Bore propagation in an trapezoidal open channel. Definition of variables: W: width of the channel, h: water depth, h_0: water depth in the axis, β: angle of the banks, U: section-averaged velocity in the axis direction, c_b: bore celerity.

allowing to point out that the LFN secondary waves are not related to the same dispersive non-hydrostatic process generating the HFN/Favre waves.

3.1 Setup

The geometry of the channel is represented by the bathymetry sketched on figure 5. Width W, angle β and water depth h_1 are the same than in [29]: $W = 1.24$ m, $\tan\beta = 1/3$, $h_1 = 0.16m$.

The jump conditions required to initialize the computations are obtained from a section-integrated version of the shallow water equations [7] :

$$
\begin{cases}
\dfrac{\partial A}{\partial t} + \dfrac{\partial Q}{\partial x} = 0 \\[2ex]
\dfrac{\partial Q}{\partial t} + \dfrac{\partial}{\partial x}\left(\dfrac{Q^2}{A} + K\right) = 0
\end{cases} ,
\tag{5}
$$

where, as in figure 5-(a), d_0 is a constant still water depth, $h_0 = d_0 + \zeta(x,t)$ is the depth associated to a wave height ζ constant along the section, $A = Wh_0 + h_0^2/\tan\beta$ is the wet section, and $Q = UA$ is the total flow rate through the wet section. For the configuration of figure 5-(a), following [7] the effective hydrostatic pressure K can be easily shown to be

$$
K = g\frac{Wh_0^2}{2} + g\frac{h_0^3}{3\tan\beta} .
\tag{6}
$$

The Rankine-Hugoniot relations become in this case:

$$
\begin{cases}
U_1 - c_b = -\left(g\dfrac{A_2}{A_1}\dfrac{K_2 - K_1}{A_2 - A_1}\right)^{1/2} \\[3ex]
U_2 - c_b = -\left(g\dfrac{A_1}{A_2}\dfrac{K_2 - K_1}{A_2 - A_1}\right)^{1/2}
\end{cases} ,
\tag{7}
$$

reducing to (3) for $\tan\beta \to \infty$. We have performed simulations for different values of the Froude number defined as

$$
Fr = \frac{|U_1 - c_b|}{\sqrt{g\bar{h}_1}} , \quad \bar{h}_1 := \frac{A_1}{\partial_h A(h_1)} = \frac{W\tan\beta + h_1}{W\tan\beta + 2h_1}h_1 .
\tag{8}
$$

The computational domain is a rectangle of dimensions $[100 \times 1.5]$ m^2 corresponding to the half of the channel width. Symmetry/reflecting boundary conditions are imposed on the axis. The initial solution is defined by the following regularization of (7):

$$\begin{cases} h(x,y,t=0) & = & \dfrac{h_2 - h_1}{2} \tanh\left(\dfrac{x - x_0}{l_t}\right) + h_2 - b(y) \\[3mm] u(x,y,t=0) & = & \dfrac{U_2 - U_1}{2} \tanh\left(\dfrac{x - x_0}{l_t}\right) + U_2 \\[3mm] v(x,y,t=0) & = & 0 \end{cases} \quad, \tag{9}$$

where $x_0 = 95$ m and $l_t = 0.5$ m, and having assumed velocities to have a uniform value across the section. Grid sizes of $\delta_x = 0.04$ m and $\delta_y = 0.05$ m, respectively in the x and y directions, are used which guarantee to have at least about 20 points per wavelength also for the shortest waves simulated.

3.2   Numerical results

Simulations have been performed for a range of Froude numbers from 1.02 to 1.275. Snapshots of the water levels obtained for four representative values of Fr are reported on figure 6. Compared to the visualization of figure 3, these pictures clearly show the complexity of the wave dynamics induced by the interaction with the sloping banks. The low Froude results look somewhat more similar to the results obtained for a rectangular section, with a wave phase structure clearly uniform along the section. As Fr increases the wave field becomes highly two-dimensional.

To further investigate this point, we have reported on figure 7 the free surface elevation along the channel axis and close to the banks. These figures allow to see clearly the transition between the LFN regime, with uniform phase structure along the section and a single dominant wavelength (figure 7-(a), and (b)), to the HFN regime in which two types of waves interact (figure 7 (c), (d), and (e)). The interaction between these two leads to the three-dimensional wave fields of the bottom pictures in figure 6. As in the field observations by [4], and as discussed in the introduction, the LFN regime is characerazed by amplitudes being higher on the banks than on the axis, while the HFN bores have larger amplitudes on the channel axis. We underline in particular the striking resemblance of the HFN bore of figure 7-(e) and of the LFN wave of figure 7-(a), with the bores measured in the Garonne river and reported respectively in figures 2-(b) and 2-(d).

To provide a more quantitative assessment of the numerical results, we have post processed the time series of the water elevation for all the simulated values of Fr to obtain the amplitude of the first peak and trough , the wavelength, and the steepness. The results are compared to the experimental data by [29] in figure 8.

The numerical peak and trough amplitude, denoted by $A_{\max}$ and $A_{\min}$ respectively, are compared to the experiments in figures 8-(a) for the channel axis, and 8(b) for the sloping banks. On the axis both experiments and simulations show a quasi-linear increase in the water elevations with the Froude number, with no clear transition. On the contrary, on the sloping banks we observe a clear transition, taking place for a value $Fr_t \approx 1.15$. Before Fr_t, the peak elevations increase more rapidly than on the axis, in agreement with the LFN signals observed in figures 7-(a) and 2-(d). In the LFN regime, the trough amplitudes $A_{\min}$ remain roughly constant. After the transition, on the sloping banks the increase of peak amplitude with Fr becomes very weak, while the trough amplitude start increasing. This leads to the HFN regime in which the amplitude on the axis are more important than those on the sloping banks, as already observed in figures 7-(e) and 2-(b) for the field measurements. The agreement between simulations and

(a) $Fr = 1.05$

(b) $Fr = 1.10$

(c) $Fr = 1.17$

(d) $Fr = 1.20$
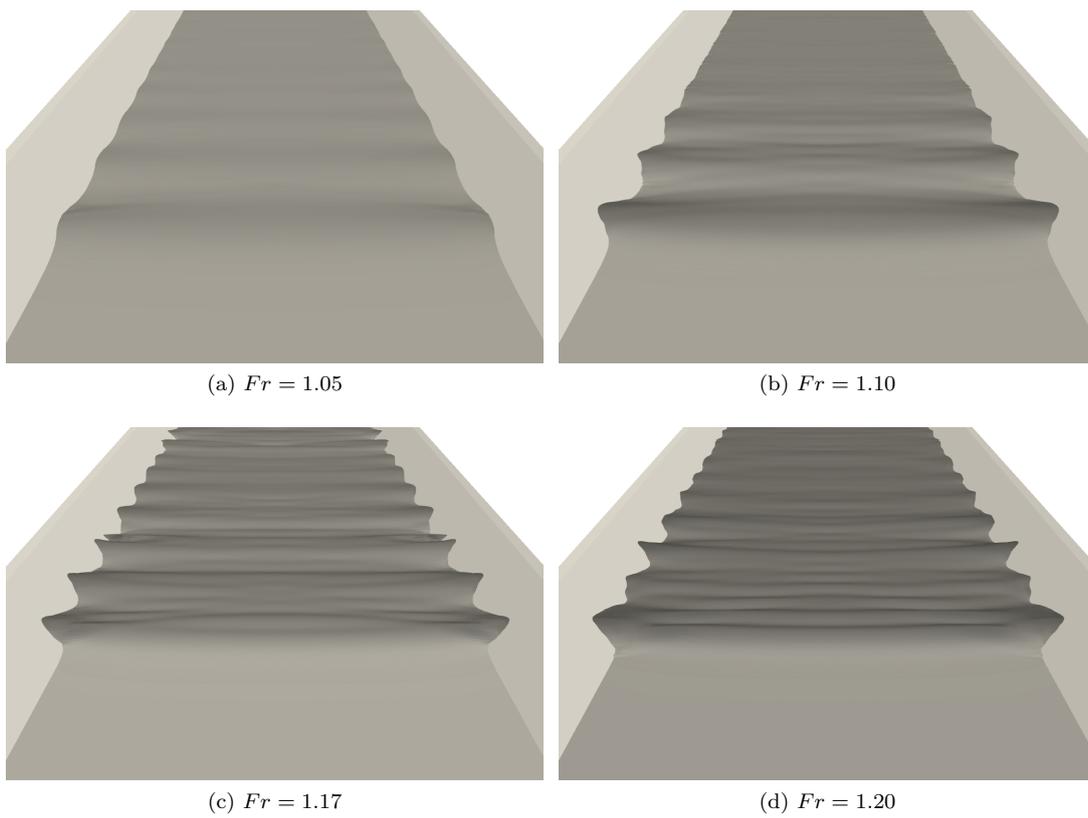
Figure 6: Snapshots of the simulated undular bores for different Froude numbers.

(a) $Fr = 1.05$

(b) $Fr = 1.10$



(c) $Fr = 1.17$

(d) $Fr = 1.20$

(e) $Fr = 1.25$
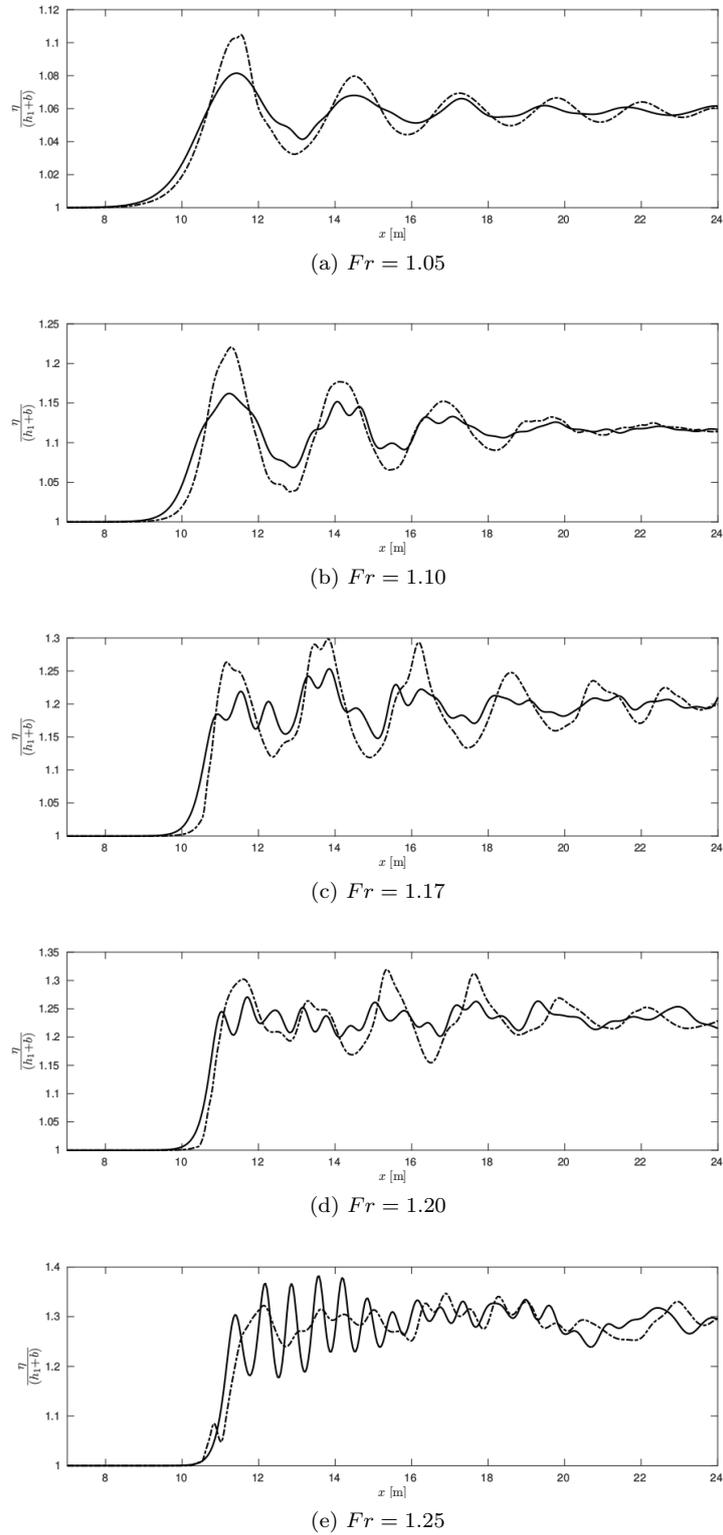
Figure 7: Free surface profiles for different Froude numbers. Continuous line: axis. Dash-dot: banks

experiment is very good, with the exception of a small advance on the onset of the transition, and of an underestimation of the slow growth of the peaks after Fr_t. This mismatch may be related to the necessity of finer meshes in this area or, more likely, to the parametrization of the wave breaking closure for which we have used standard values from [16], and did not try to optimize.

The transition between the LFN and HFN bores can be seen very clearly in the wavelength and steepness distributions, reported in figures 8-(c) and 8-(d) respectively. For these quantities the agreement between simulations and experimental data is excellent. We can see that the HFN regime is characterized by wavelengths on the axis very close to those observed in straight channels. This is made more clear by reporting in the figure the values computed by means of the theory by [21]. The curve provides a very good fit of the wavelengths observed in the simulations and in the experiments. This suggests that non-hydrostatic dispersive effects are the dominating ones on the channel axis, as in Favre waves. On the sloping banks some other phenomenon is active, as the wavelengths observed are about 3 times larger than on the axis. This leads to wave signals as those reported on figures 7-(c) and 7-(d). Below Fr_t both on the axis and on the sloping banks wavelengths have values 3 or 4 times larger than those predicted by the theory of [21]. In the LFN regime, the trend with the Froude number is the same observed on the banks for HFN waves. The distribution of the steepness $(A_{\max} - A_{\min})/2\lambda$ on the channel axis, reported for completeness in figure 8-(d), also allows to see the transition between the LFN and HFN waves. Very similar results with field data from the Garonne and Seine rivers field measurements can be found in [4].

The overall agreement between simulations and experiments is very good, showing that weakly dispersive Serre-Green-Naghdi modelling is adequate to capture the complex wave dynamics discussed. The main question remaining open is the origin of the LFN bores. The objective of the remainder of this paper is to propose a dispersive-like mechanism for these waves.

4   Dispersive-like mechanism for small Froude numbers

4.1   Motivation

This section discusses one of the main results of this paper. We will show that the dispersion characteristics of LFN waves can be modelled by a fully hydrostatic section-averaged model, obtained starting from the shallow water equations. The dispersive effects embedded in this model are purely hydrostatic and related to the refraction along the banks. For this reason we speak of a *dispersive-like* process.

Note that waves with characteristics somewhat similar to those observed here are the well known edge waves for which there exist a certain number of analytical solutions obtained from the full potential equations. The interested reader may consult for example the works of [30, 22] and more recently [15], and references therein.

As in the case of edge waves, we claim that the main physical mechanism acting here is refraction induces by the sloping banks. To give a theoretical characterization of the LFN waves here we claim that we can start from an appropriately scaled linearized shallow water approximation. Indeed, dispersive propagation has been shown to arise for sandard linear waves in heterogeneous media [9, 18]. For the application considered here, our intuition is related to two observations. First, the LFN waves are much longer than the standard Favre waves. Second, in the HFN regime these waves can still be observed in trapezoidal channels on the sloping banks where the non-hydrostatic effects are known to be less relevant. To verify this intuition, we propose a first experiment consisting in repeating the simulations of section §3 with the shallow water equations. The results are summarized on figure 9. The left picture in the figure shows

(a) Water elevation (axis)

(b) Water elevation (banks)

(c) Wavelength

(d) Steepness (axis)
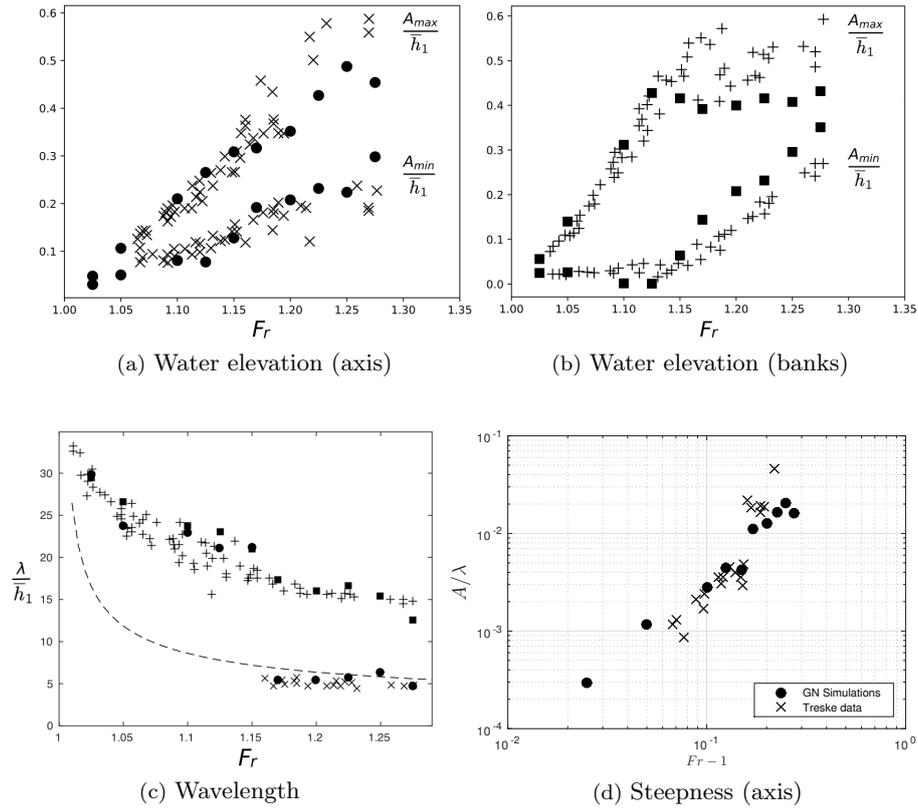
Figure 8: Wavelength and water level of the undular bores in a channel with trapezoidal section. $\times$: Data of [29] axis, $+$: Data of [29] banks, $\bullet$: simulated values on the channel axis, $\blacksquare$: simulated values on the banks, $--$: [21] theory
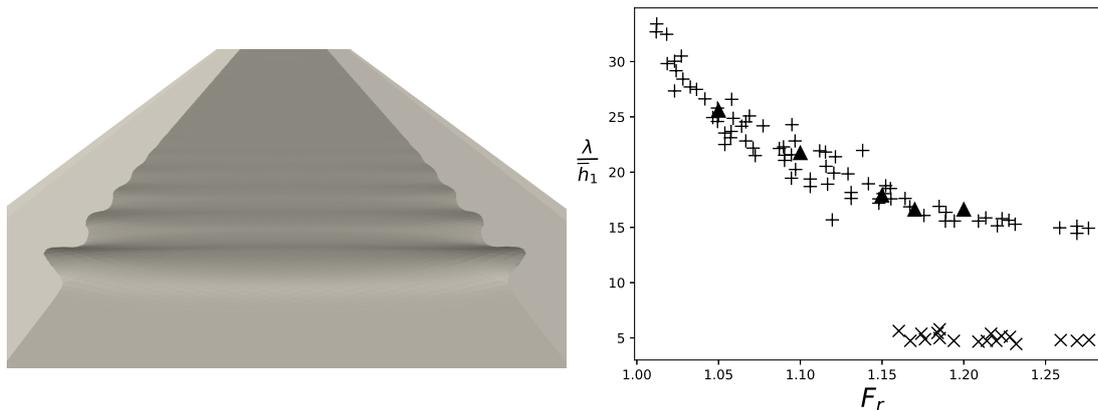
Figure 9: Numerical verification: Treske experiments reproduced with shallow water simulations. Left: free surface for $Fr = 1.15$. Right: comparison of computed wavelengths (▲) with the data from the experiment by Treske (+ : banks, × : axis).

the free surface profile obtained numerically for $Fr = 1.05$. The presence of undulations in the propagation is clearly visible. Also, these features do not disappear as the mesh is refined. The right picture in the figure shows the comparison of the wavelengths measured in the shallow water simulations with the data of Treske. The hydrostatic model clearly reproduces the LFN waves. Also note that the wavelengths measured are the same on the banks and on the axis, as one would expect.

Tom complete the study, in the following we discuss an asymptotic and section-averaged approximation of the linear hydrostatic shallow water equations exhibiting *geometrical dispersion*. To obtain this result we make the hypothesis that a fast wave refraction phenomenon is present in the transversal direction. The time scale associated to this phenomenon, denoted by τ_y is thus assumed to be much smaller than the time scale in the propagation direction, denoted by τ_x. This hypothesis implies the existence of a small parameter defined as the ratio between the transversal and longitudinal time scales or, equivalently, as the reference length ratio

$$\delta := \frac{\tau_y}{\tau_x} \approx \frac{L_y}{L_x} \ll 1 \tag{10}$$

The correctness of our asymptotic approximation is first verified against numerical computations of monochromatic waves, and finally applied to the experiments of Treske by means of an analysis similar to the one performed in [21].

4.2   Hydrostatic section-averaged approximation

Consider the geometrical configuration depicted on figure 10. We are interested in deriving a linear approximate model for the evolution of the section-averaged free surface, where the section-averaging operator is denoted by an over-line, and defined by

$$\overline{(\cdot)} = \frac{1}{2y_0} \int_{-y_0}^{y_0} (\cdot) \, dy \tag{11}$$
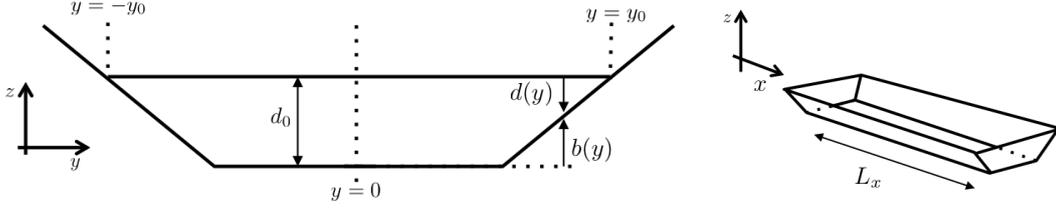
Figure 10: Main geometrical notation for the asymptotic analysis.

An exception to the above notation is the section-averaged depth at still water, which we denote by h_0. Using the notation of figure 10, we have that

$$h_0 = \overline{d} = d_0 - \overline{b} \tag{12}$$

We also denote $C_0^2 = gh_0$ the square celerity corresponding to h_0. Let now L_y be the half channel breadth at the still water level, a a reference wave height, and $\epsilon = a/h_0$ the standard non-linearity parameter. We consider the following dimensionless form of the main physical variables (cf. figure 10):

$$\partial x' = \frac{\partial x}{L_x}, \quad \partial y' = \frac{\partial y}{L_y}$$

$$b' = \frac{b}{h_0}, \quad \zeta' = \frac{\zeta}{a}, \quad d' = \frac{d}{h_0} \tag{13}$$

$$t' = \frac{C_0}{L_x}t, \quad u' = \frac{u}{\epsilon C_0}, \quad v' = \frac{v}{\epsilon C_0}$$

In the above equations we recall that u and v denote the components of the depth averaged flow speed for which the dimensional scaling by ϵC_0 is a classical choice (see e.g. [10, 19]). The quantity y_0, required for the evaluation of the section average, is the actual time-/space-dependent half-breadth corresponding to the local position of the water line. This means that

$$y_0 = L_y + \int_0^t v\big|_{y=y_0}\, \mathrm{d}t \rightarrow y_0' = 1 + \frac{\epsilon}{\delta}\Delta_y, \quad \Delta_y := \int_0^{t'} v'\big|_{y'=y_0'}\, \mathrm{d}t' \tag{14}$$

We now consider the nonlinear shallow water equations in dimensionless form

$$\partial_t \zeta + \partial_x\big((d+\epsilon\zeta)u\big) + \frac{1}{\delta}\partial_y\big((d+\epsilon\zeta)v\big) = 0$$

$$\partial_t u + \epsilon u \partial_x u + \frac{\epsilon}{\delta}v\partial_y u + \partial_x \zeta = 0 \tag{15}$$

$$\partial_t v + \epsilon u \partial_x v + \frac{\epsilon}{\delta}v\partial_y v + \frac{1}{\delta}\partial_y \zeta = 0$$

Note that the primes have been dropped to simplify the notation. For simplicity we assume unduly that the flow is fully symmetric w.r.t. the channel centerline $y = 0$. On the banks, the equations satisfy the boundary conditions

$$\pm y = y_0 + \frac{\epsilon}{\delta}\Delta_y \Rightarrow (d+\epsilon\zeta)v = 0, \quad (d+\epsilon\zeta)u = 0, \quad d+\epsilon\zeta = 0 \tag{16}$$

The condition on $(d + \epsilon\zeta)v$ also applies to channels with vertical side walls.

We now pass to a fully linear regime $\epsilon \to 0$. Equation (14) allows to simplify the domain definition in the transversal direction which is now $y \in [-1, \ 1]$. This allows to simplify the section-averaging operator which becomes

$$\overline{(\cdot)} = \frac{1}{2} \int_{-1}^{1} (\cdot) \, \mathrm{d}y \ . \tag{17}$$

The linearized model equations read

$$\partial_t \zeta + d\partial_x u + \frac{1}{\delta} \partial_y (dv) = 0$$

$$\partial_t u + \partial_x \zeta = 0$$

$$\partial_t v + \frac{1}{\delta} \partial_y \zeta = 0 \tag{18}$$

$$y = \pm 1 \to dv = 0$$

where the last expression is a linear non-dimensional boundary condition, still valid for both banks and vertical side walls.

The boundary condition in (18) can be readily used to derive a section-averaged wave equation by taking the average of the first in (18):

$$\begin{cases} \partial_t \overline{\zeta} + \overline{d\partial_x u} = 0 \\ \\ \partial_t u + \partial_x \zeta = 0 \end{cases} \Rightarrow \partial_{tt} \overline{\zeta} - \overline{d\partial_{xx}\zeta} = 0 \tag{19}$$

Our objective is to obtain a closed form of the above equation for the evolution in space and time of $\overline{\zeta}$. To this end we invoke hypothesis (10), and we introduce asymptotic expansions of all the variables in terms of the small parameter δ:

$$\begin{cases} \zeta = \zeta_0 + \delta\zeta_1 + \delta^2\zeta_2 + \ldots \\ u = u_0 + \delta u_1 + \delta^2 u_2 + \ldots \\ v = v_0 + \delta v_1 + \delta^2 v_2 + \ldots \end{cases} \tag{20}$$

These expansions are substituted in (18), and terms of equal powers in δ are equated. This results in a system of partial differential relations/equations for the coefficients in the development. This system can be closed applying iteratively the three following steps:

1. $\partial_y(dv_{n+1}) = -(\partial_t \zeta_n + d\partial_x u_n)$, with $dv_{n+1} = 0$ for $y = \pm 1$;

2. $\partial_t u_n = -\partial_x \zeta_n \ , \ \forall \, n$;

3. $\partial_y \zeta_{n+1} = -\partial_t v_n$

To complete the procedure, we need a starting condition as well as a way of closing the integration along y required in step (iii) (for step (i) the boundary condition provides this closure).

The starting condition is obtained by observing that $\partial_y(dv_0) = 0$ with $dv_0 = 0$ on both sides of the domain. This implies $v_0 = 0$ which is used as initial value in (i) and (iii).

Concerning the step (iii), the closure used here is based on the explicit computation of a primitive function Z_{n+1} such that $\partial_y Z_{n+1} = -\partial_t v_n$. This means that

$$\zeta_{n+1} = Z_{n+1} + F(x,t)$$

Note that in general $Z_{n+1} = Z_{n+1}(x,y,t)$. We express the integration "constant" F using section-averaged values: $F = \overline{\zeta}_{n+1} - \overline{Z}_{n+1}$. This gives the closure for step (iii):

$$\zeta_{n+1} = \overline{\zeta}_{n+1} + Z_{n+1} - \overline{Z}_{n+1}$$

Applying this procedure we obtain the following order results.

Order 0

$$v_0 = 0$$
$$\zeta_0 = \overline{\zeta}_0(x,t) \tag{21}$$

Order 1

$$v_1 = -\frac{1+y}{d}\partial_t\overline{\zeta}_0 - \frac{D}{d}\partial_x\overline{u}_0\,, \quad D = \int_{-1}^{y} d(s)\mathrm{d}s$$
$$\zeta_1 = \overline{\zeta}_1(x,t) \tag{22}$$

Order 2

$$v_2 = -\frac{1+y}{d}\partial_t\overline{\zeta}_1 - \frac{D}{d}\partial_x\overline{u}_1\,, \quad D = \int_{-1}^{y} d(s)\partial s$$
$$\zeta_2 = \overline{\zeta}_2(x,t) + (\kappa(y) - \overline{\kappa})\partial_{xx}\overline{\zeta}_0\,, \quad \kappa(y) = \int_{-1}^{y} \frac{1+s-D(s)}{d(s)}\,\mathrm{d}s \tag{23}$$

Order 3

$$v_3 = -\frac{1}{d}\int_{-1}^{y}(\partial_t\eta_2 + d\partial_x u_2)\partial s$$
$$\zeta_3 = \overline{\zeta}_3(x,t) + (\kappa(y) - \overline{\kappa})\partial_{xx}\overline{\zeta}_1\,, \quad \kappa(y) = \int_{-1}^{y} \frac{1+s-D(s)}{d(s)}\,\mathrm{d}s \tag{24}$$

We do not proceed further as the above solutions allow to provide an approximation which is exact within an order $\mathcal{O}(\delta^4)$. This is the typical order retained for weakly dispersive models as e.g. the Serre-Green-Naghdi model used in this paper. Collecting all the orders, we have

$$\zeta = \overline{\zeta}_0 + \delta\overline{\zeta}_1 + \delta^2\left(\overline{\zeta}_2 + (\kappa(y) - \overline{\kappa})\partial_{xx}\overline{\zeta}_0\right) + \delta^3\left(\overline{\zeta}_3 + (\kappa(y) - \overline{\kappa})\partial_{xx}\overline{\zeta}_1\right) + \mathcal{O}(\delta^4)$$

Using the relations $\zeta = \zeta_0 + \delta\zeta_1 + \mathcal{O}(\delta^2)$ and that $\overline{\zeta}_0 + \delta\overline{\zeta}_1 + \delta^2\overline{\zeta}_2 + \delta^3\overline{\zeta}_3 = \overline{\zeta} + \mathcal{O}(\delta^4)$, we deduce the following asymptotic expansion for the free surface:

$$\zeta = \overline{\zeta} + \delta^2(\kappa(y) - \overline{\kappa})\partial_{xx}\overline{\zeta} + \mathcal{O}(\delta^4) \tag{25}$$

We can now use this expansion in the section-averaged wave equation (19) to obtain, within a $\mathcal{O}(\delta^4)$ error, the following section-averaged dispersive approximation

$$\partial_{tt}\overline{\zeta} - \partial_{xx}\overline{\zeta} - \delta^2\chi\partial_{xxxx}\overline{\zeta} = 0 \tag{26}$$

The coefficient χ is a *geometrical dispersion coefficient* defined by

$$\chi = \overline{d(y)\kappa(y)} - \overline{d}\,\overline{\kappa} \tag{27}$$

with the expression for $\kappa(y)$ provided both in (23) and (24). We stress that this dispersive perturbation is only related to the geometrical shape of the channel section, and to the initial hypothesis that $\delta \ll 1$. We recall that this hypothesis implies that the transversal time/length scale, related to the wave refraction, is much smaller than the time/length scale in the main propagation direction.

By means of standard Fourier transform, we can easily obtain the dispersion relation verified by solutions of (26), which reads in dimensional form

$$\omega^2 = k^2 C_0^2 \big(1 - \chi(kL_y)^2\big) \tag{28}$$

with k the wavenumber.

4.3 Numerical verification of the expansion for monochromatic waves

Our first objective is to verify the asymptotic approximation obtained. This is not a completely trivial task, as we do not have any analytical reference to compare to. To perform this verification, we compare the dispersion characteristics of the asymptotic model to those obtained numerically on fine meshes with the code described in section §2.1 in the shallow water limit.

Setting $\overline{\zeta} = a\sin(k\,x - \omega\,t)$ we can deduce for a given channel a y dependent boundary condition from (25). This is used as an inlet condition in the code. To avoid the impact of the treatment of the wet-dry interface, in the computations the bathymetry is modified introducing vertical lateral walls, as depicted on figure 11. Note that, as remarked several times, this configuration is also compatible with the boundary condition used in the asymptotic development. The computations are started from a flat free surface, and the inlet boundary condition is propagated numerically in the channel. The numerical solution obtained is then averaged over the section and the resulting signal analyzed to measure the dispersion relation provided by the simulations. Note that these results embed full nonlinearity and a full approximation of the transverse propagation. For this reason they are considered as a good reference against which the theoretical relation (28) can be tested.

The resulting comparisons are reported on figure 12 for trapezoidal and triangular channels in terms of non-dimensional celerity and phase. The figure highlights two things. First, a dispersive process is indeed present in the shallow water results. Secondly, for long waves, namely $kL_y \leq 5-6$, the asymptotic approximation provides an excellent prediction of the physical dispersion relation. This allows to verify the soundness of the asymptotic development, and implicitly confirms the geometrical origin and hydrostatic nature of the dispersive behaviour observed. For this reason we speak here of *dispersive-like* waves, as actual physical non-hydrostatic/dispersive effects are not the origin of these waves.
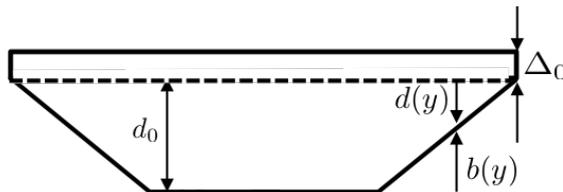
Figure 11: Channel geometry used for the numerical verification.

Concerning the deviation observed for higher wave numbers for the triangular shape may be related to the effects neglected in the asymptotic development (e.g. some geometrical nonlinearity to account for higher bank slopes).

4.4   Application to LFN bores

We propose here a method to predict the wavelength observed in the LFN regime in the spirit of [21]. Using the linearized dispersive model derived in the previous sections, we compute theoretical wavelengths by equating the bore speed obtained from the jump conditions (7) with the celerity in (28):

$$C_0^2 \left(1 - \chi(kL_y)^2\right) = g\frac{A_1}{A_2}\frac{K_2 - K_1}{A_2 - A_1} \tag{29}$$

For a given Froude number, the above equation can be readily solved for the wavelength $\lambda = 2\pi/k$. The resulting wavelength distribution w.r.t. the Froude number is plotted in figure 13 against both the data by Treske, and the shallow water (left) and Serre-Green-Naghdi (right) simulations.

The results clearly shows that our theoretical analysis fully captures the nature of the LFN waves. They confirm that the low Froude waves observed in the experimental setting by [29], and those of the field measurements by [4] have an entirely different nature from the so called Favre waves. The latter are associated to fully non-hydrostatic dispersion, while LFN bores are mainly related to the coupling of geometrical refraction in the transversal direction and hydrostatic wave propagation.

5   Conclusions and outlook

In this paper we have proposed a detailed analysis of undular bore dynamics in channels of variable cross-section. By means of a weakly-dispersive Serre-Green-Naghdi numerical model we have successfully reproduced the two undular bore regimes, a Low Froude Number (LFN) and a High Froude Number (HFN) one, observed both in the experiments by [29] and in [4] in field measurements in the Garonne and Seine rivers. In the HFN regime two family of waves are observed. On the channel axis short waves with characteristics similar to those of the well known Favre waves. These are associated to non-hydrostatic dispersive effects. On the sloping banks, longer waves are observed, clearly not generated by the same phenomenon. The interaction between these two leads to a complex two-dimensional wave phase structure. In the LFN regime, only the long waves are observed in the whole channel. This gives a quasi one-dimensional wave phase structure, with larger amplitudes on the banks. A dispersive-like mechanism related to geometrical refraction on the banks has been proposed as the phenomenon responsible for the LFN waves. The claim has been first verified numerically, showing that these waves can be reproduced with shallow water simulations. Then we have shown that, under the hypothesis
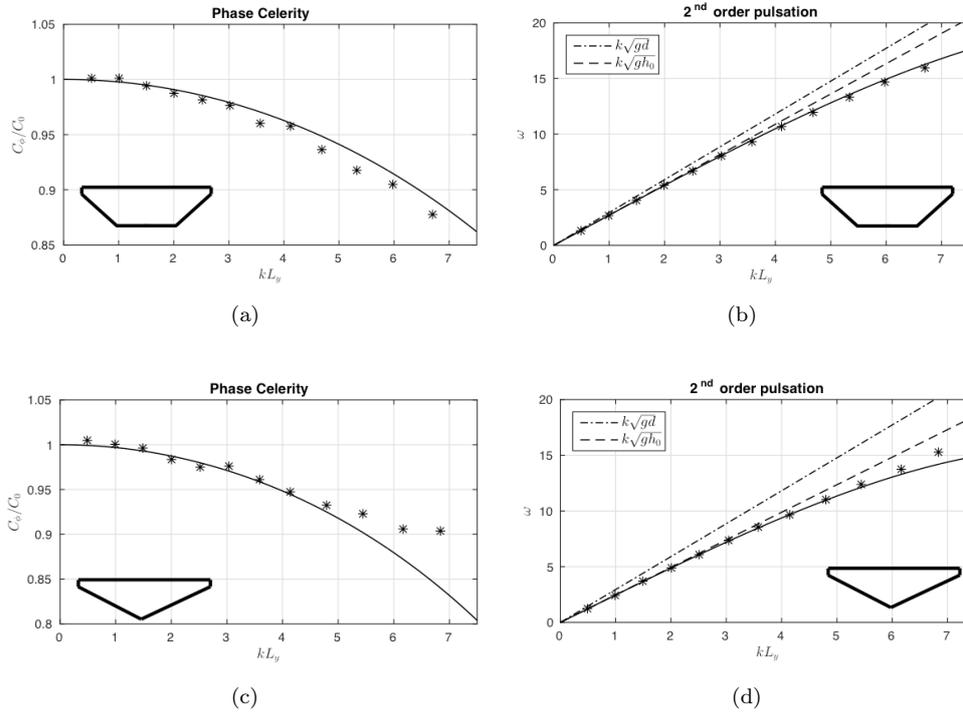
Figure 12: Verification of the asymptotic analysis: trapezoidal (top) and triangular (bottom) section. Left: celerity. Right: phase. $*$: shallow water code; —— : new asymptotic theory; $---$: linear phase for $d(y) = \overline{d}$; $-\cdot-$: linear phase phase for $d(y) = d_0$.
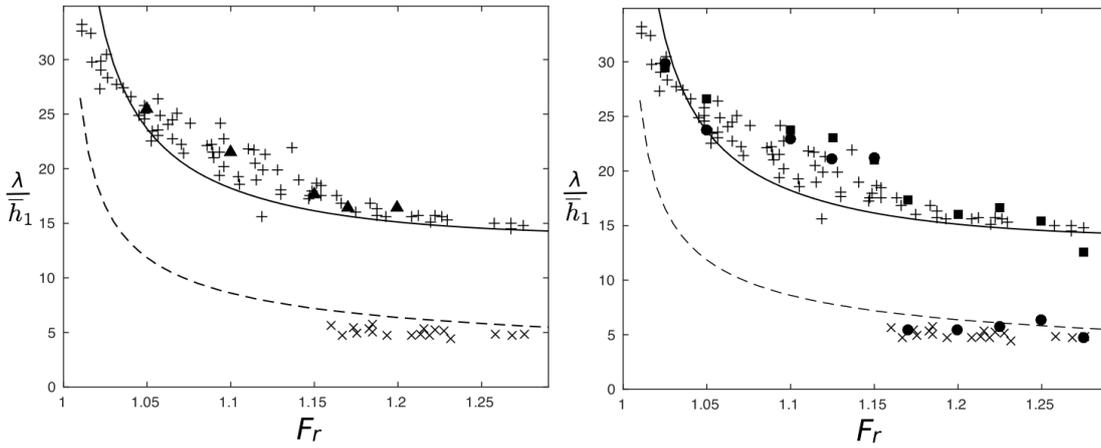

Figure 13: Theoretical wavelengths compared to numerical and experimental data. $\times$: data of [29] axis, $+$: data of [29] banks, $\bullet$: Serre-Green-Naghdi simulations axis, $\blacksquare$: Serre-Green-Naghdi simulations banks, $\blacktriangle$: shallow water simulations, $--$: [21] theory, —— : new asymptotic theory.

that the time scale associated to refraction in the transversal direction is much smaller than the time scale associated to wave propagation, the section averaged free surface level verifies a linear dispersive wave equation. The corresponding dispersion relation has been used to compute theoretical wave lengths of the secondary waves and show to fit very accurately the wavelengths observed in the LFN regime.

This study clears the main mechanism active in the LFN regime. However, it remains to understand what are the mechanisms leading the transition between LFN and HFN waves. It will be also interesting to understand the dependence of the LFN waves on the geometrical parameters of the channel. Preliminary investigations have shown that wavelengths in the LFN regime decrease as the slope of the banks β or when the channel width W increase (cf. figure 5(a)), while the same parameters have a small impact in the HFN regime. A detailed study of these issues, as well as a numerical and theoretical analysis of realistic configurations as those studied in [4] are currently ongoing.

Acknowledgements

A Differential operators defining the non-hydrostatic correction

The differential operators appearing in (2) can be recast as

$$
\mathrm{T}(\boldsymbol{\omega}) = -\frac{1}{3}\nabla\left(h^3\nabla\cdot\left(\frac{\boldsymbol{\omega}}{h}\right)\right) - \frac{h^2}{2}\left(\nabla\cdot\left(\frac{\boldsymbol{\omega}}{h}\right)\right)\nabla b +
$$
$$
+\ \frac{1}{2}\nabla\left(h^2\nabla b\cdot\left(\frac{\boldsymbol{\omega}}{h}\right)\right) + h\left(\nabla b\cdot\left(\frac{\boldsymbol{\omega}}{h}\right)\right)\nabla b \ , \tag{30}
$$

$$
\mathrm{Q}(\boldsymbol{\omega}) = \frac{2}{3}\nabla\left(h^3\left(\nabla\omega_1\cdot\nabla^\perp\omega_2 + \left(\nabla\cdot\boldsymbol{\omega}\right)^2\right)\right) +
$$
$$
+\ h^3\left(\nabla\omega_1\cdot\nabla^\perp\omega_2 + \left(\nabla\cdot\boldsymbol{\omega}\right)^2\right)\nabla b +
$$
$$
+\ \frac{1}{2}\nabla\left(h^2\left(\boldsymbol{\omega}\cdot\left(\boldsymbol{\omega}\cdot\nabla\right)\nabla b\right)\right) + h\left(\boldsymbol{\omega}\cdot\left(\boldsymbol{\omega}\cdot\nabla\right)\nabla b\right)\nabla b \ , \tag{31}
$$

where b represents the bathymetry, ω_1 and ω_2 denote the first and second component of the vector $\boldsymbol{\omega}$, and $\nabla^\perp$ denotes the orthogonal of the gradient operator.

References

[1] B. Alvarez-Samaniego and D. Lannes. A Nash-Moser theorem for singular evolution equations. Application to the Serre and Green-Naghdi equations. *Indiana University Mathematics Journal*, 57(1), 2008.

[2] N. Bonneton, P. Bonneton, J.-P. Parisot, A Sottolichio, and G Detandt. Tidal bore and Mascaret - example of Garonne and Seine Rivers. *Comptes Rendus Geosciences*, 344(508-515), 2012.

[3] P. Bonneton. Modelling of periodic wave transformation in the inner surf zone. *Ocean Engineering*, 34(10):1459 – 1471, 2007.

[4] P. Bonneton, N. Bonneton, J.-P. Parisot, and B. Castelle. Tidal bore dynamics in funnel-shaped estuaries. *Journal of Geophysical Research: Oceans*, 120(2):923–941, February 2015.

[5] P Bonneton, J Van de Loock, J-P Parisot, N Bonneton, A Sottolichio, G Detandt, B Castelle, V Marieu, and N Pochon. On the occurrence of tidal bores – The Garonne River case. *Journal of Coastal Research*, (64):6, 2011a.

[6] Philippe Bonneton, Jean-Paul Parisot, Natalie Bonneton, Aldo Sottolichio, Bruno Castelle, Vincent Marieu, Nicolas Pochon, and Van de Loock. Large Amplitude Undular Tidal Bore Propagation in the Garonne River, France. *Proc. of the 21st ISOPE Conference*, pages 870–874, 2011b.

[7] Hubert Chanson. *Hydraulics of Open Channel Flow - 2nd Edition*. 2004.

[8] F. Chazel, D. Lannes, and F. Marche. Numerical simulation of strongly nonlinear and dispersive waves using a Green–Naghdi model. *J.Sci.Comput.*, 48(3), 2011.

[9] Manuel Quezada de Luna and David I. Ketcheson. Two-dimensional wave propagation in layered periodic media. *arXiv:1309.6666 [math]*, September 2013.

[10] M.W. Dingemans. *Water Wave Propagation Over Uneven Bottoms: Linear wave propagation.* Advanced series on ocean engineering. World Scientific Pub., 1997.

[11] Henry Favre. *Étude théorique et expérimentale des ondes de translation dans les canaux découverts.* Dunod, 1935.

[12] A. G. Filippini, M. Kazolea, and M. Ricchiuto. A flexible genuinely nonlinear approach for nonlinear wave propagation, breaking and run-up. *Journal of Computational Physics*, 310(Supplement C):381–417, April 2016.

[13] Andrea Gilberto Filippini, Maria Kazolea, and Mario Ricchiuto. A Flexible 2D Nonlinear Approach for Nonlinear Wave Propagation, Breaking and Run up. In *Proceedings of the Twenty-seventh (2017) International Ocean and Polar Engineering Conference (ISOPE), www.isope.org - ISBN 978-1-880653-97-5; ISSN 1098-6189*, pages 1323–1331, San Francisco, CA, United States, June 2017.

[14] Andrea Gilberto Filippini, Maria Kazolea, and Mario Ricchiuto. Hybrid finite-volume/finite-element simulations of fully-nonlinear/weakly dispersive wave propagation, breaking, and runup on unstructured grids. In *SIAM Conference on Mathematical and Computational Issues in the Geosciences*, Erlangen, Germany, September 2017.

[15] R. S. Johnson. Edge waves: theories past and present. *Philosophical Transactions of the Royal Society of London A: Mathematical, Physical and Engineering Sciences*, 365(1858):2359–2376, September 2007.

[16] M. Kazolea, A. I. Delis, and C. E. Synolakis. Numerical treatment of wave breaking on unstructured finite volume approximations for extended Boussinesq-type equations. *Journal of Computational Physics*, 271(Supplement C):281–305, August 2014.

[17] M. Kazolea and M. Ricchiuto. On wave breaking for Boussinesq-type models. *Ocean Modelling*, 123:16–39, March 2018.

[18] D. Ketcheson and M. Quezada de Luna. Diffractons : Solitary Waves Created by Diffraction in Periodic Media. *Multiscale Modeling & Simulation*, 13(1):440–458, January 2015.

[19] D. Lannes. The water waves problem. Mathematical analysis and asymptotics. Mathematical Surveys and Monographs. Americal Mathematical Society, 2013.

[20] David Lannes and Fabien Marche. A new class of fully nonlinear and weakly dispersive Green-Naghdi models for efficient 2d simulations. *Journal of Computational Physics*, pages 238–268, December 2014.

[21] R. Lemoine. Notules hydrauliques. *La Houille Blanche*, (2):183–186, March 1948.

[22] J. Miles. Edge waves on a gently sloping beach. *Journal of Fluid Mechanics*, 199:125–131, 1989.

[23] D. H. Peregrine. Calculations of the development of an undular bore. *Journal of Fluid Mechanics*, 25(02):321, June 1966.

[24] F. Shi, J. T. Kirby, J. C. Harris, J. D. Geiman, and S. T. Grilli. A high-order adaptive time-stepping tvd solver for boussinesq modeling of breaking waves and coastal inundation. *Ocean Modelling*, 43-44:36–51, 2012.

[25] M Tissier, P Bonneton, F Marche, F Chazel, and D Lannes. Nearshore Dynamics of Tsunami-like Undular Bores using a Fully Nonlinear Boussinesq Model. *Journal of Coastal Research*, (64):5, 2011.

[26] M. Tissier, P. Bonneton, F. Marche, F. Chazel, and D. Lannes. A new approach to handle wave breaking in fully non-linear Boussinesq models. *Coastal Engineering*, 67(Supplement C):54–66, September 2012.

[27] Marion Tissier. *Etude numérique de la transformation des vagues en zone littorale, de la zone de levée aux zones de surf et de jet de rive.* Bordeaux 1, December 2011.

[28] M. Tonelli and M. Petti. Hybrid finite-volume finite-difference scheme for 2DH improved Boussinesq equations. *Coast. Eng.*, 56:609–620, 2009.

[29] A. Treske. Undular bores (favre-waves) in open channels - Experimental studies. *Journal of Hydraulic Research*, 32(3):355–370, May 1994.

[30] F. Ursell. Edge waves on a sloping beach. *Proceedings of the Royal Society of London. Series A, Mathematical and Physical Sciences*, 214:79–97, 1952.

[31] Ge Wei, James T. Kirby, Stephan T. Grilli, and Ravishankar Subramanya. A fully nonlinear Boussinesq model for surface waves. Part 1. Highly nonlinear unsteady waves. *Journal of Fluid Mechanics*, 294:71–92, July 1995.